# Numerical Modeling Study of Cooling Water Recirculation

Jianhua Jiang[1] and David B. Fissel[1]

## Abstract

A three-dimensional, finite difference coastal circulation numerical model, ASL-COCIRM, was adapted to examine the possible recirculation of cooling water in the Burrard Generating Station, Canada. The model resolved the near-field zone of the cooling water buoyant jet and intake using a very fine grid size (2.5 m by 2.5 m in the horizontal), which allowed the cooling water outlet pipe and intake to be represented in a realistic manner. The near-field model was then nested within the large model domain of the far-field zone of cooling discharge receiving water. Model calibration and verification results demonstrate that the model has the capability of adequately capturing the overall behavior of the buoyant jet and quantitatively investigating the waste heat recirculation into the intake and the consequent effect on the efficiency of power plants.

## Introduction

The possibility of recirculation of waste heat into cooling water intakes is of particularly concern to coastal engineers in building thermal or nuclear power stations because of its adverse impacts on the plant efficiency and operation. However, quantitative identification of such potential recirculation remains difficult due to the complicated buoyancy processes and hydrothermal features within the near-field of cooling water discharges, especially with a submerged buoyant jet. In the presence of this submerged heated buoyant jet, the receiving water exhibits large gradients in the hydrothermal field and much different spatial scales between the near-field and far-field zones, on order of $10 - 100$ m in the near-field and $1 - 10$ km in the far-field. In the recent study of the Burrard Generating Station cooling water recirculation by the authors of this paper (Jiang, et al., 2001), the potential recirculation of waste heat into the shallow coastal waters was quantitatively examined using a three-dimensional coastal circulation model, ASL-COCIRM. The model incorporated a newly developed nested grid scheme to resolve the large hydrothermal gradient in the near-field and to represent the cooling water intake and outlet in a realistic manner. The near-field model was embedded within the spatially larger and coarser grid of the far-field model. The complete field was then solved with a single modeling procedure at

---

every time step. In this paper, we use the nested model formulation to investigate the degree of direct recirculation of discharged cooling water into the intake of the plant cooling water system. We present the methodology and key model results concerning cooling water recirculation.

**Cooling Water Structure and Receiving Waters**

The Burrard Generating Station (BGS) is located on the north shore of the Port Moody Arm (hereafter, simply called the Arm), at the eastern end of the Burrard Inlet, Canada (Figure 1). The Arm has a length of 6.5 km, a mean width of 0.9 km, and the mean water depth varies from 5 to 30 m in mid-channel. A mixed tide occurs with a mean tidal range of 3 m. Tidal currents are typically 10 – 20 cm/s or less. The tidal prism is $12.2 \times 10^6$ m$^3$, which represents approximately one-third of the total volume of the Arm (Fissel, et al., 1998). The BGS releases a large volume of heated cooling water into the Arm. Under existing operating permits, the maximum allowable discharge is $1.7 \times 10^6$ m$^3$/d with a maximum temperature of 27 ℃. The cooling water temperature exceeds the temperature of the ambient water by about 4 – 10 ℃ in summer and up to 20 ℃ in winter. The maximum allowable daily discharge is about 14% of the tidal prism, and approximately 4% of the volume of water in the Arm.
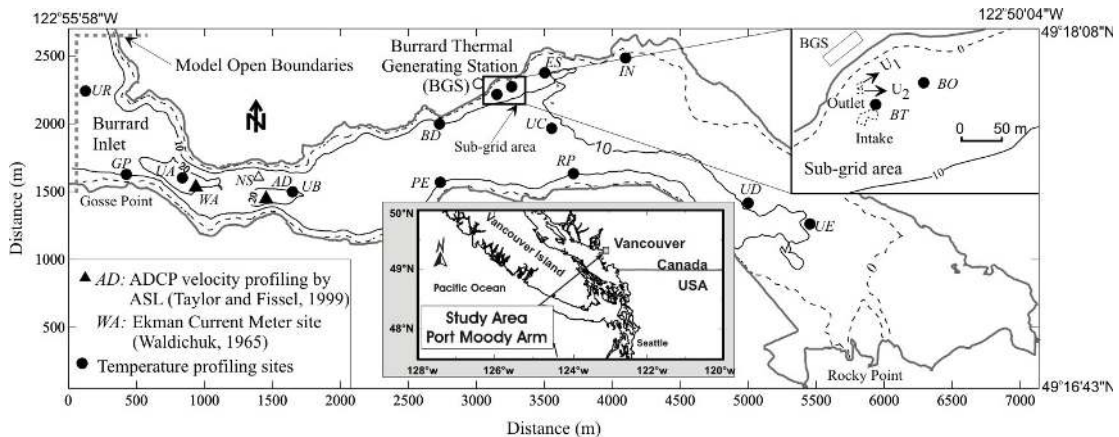


**Figure 1.** Location map of the Port Moody Arm, cooling water outlet and intake, and survey sites of temperature and currents. Depths are in meters below lowest astronomical tide.

The cooling water discharge is released into the Arm through two independent outlet systems, each consisting of a pair of adjacent horizontal pipes of diameter 2.45 m, respectively denoted the shoreward and seaward pipes, and takes the form of a submerged horizontal heated buoyant jet in a relatively shallow water depth of approximately 10 m (Figure 2). The two side pipes are set in an identical horizontal plane with a spacing of 3 – 4 m. The heights of the outlet pipes above the seabed are 6 m for the seaward pipes and about 3 m for the shoreward pipes. The exit flow from the seaward pipes is due east. The shoreward pipe flow is directed along the shoreline, resulting in an exit flow at an angle of 20° to the east (Figure 2). The

cooling water intake is located about 30 m SSE of the outlet pipe (Figure 2) in a depth of about 11 m, and has an opening at the height of 1.54 − 5.88 m above the seabed with the sides facing the outlet being closed. For safety reason, a floating boom is installed at about 70 m eastern of the outlet pipe. The boom is always floating at the water surface and has no considerable effect on flows. Extensive data sets, including temperature profiling at near-shore locations, and an ADCP and other current meter time series data, have been collected in the Arm (Fissel, et al., 1998; Taylor, et al., 1999; Birtwell, et al., 2001). These data sets have been used for model calibration and verification.
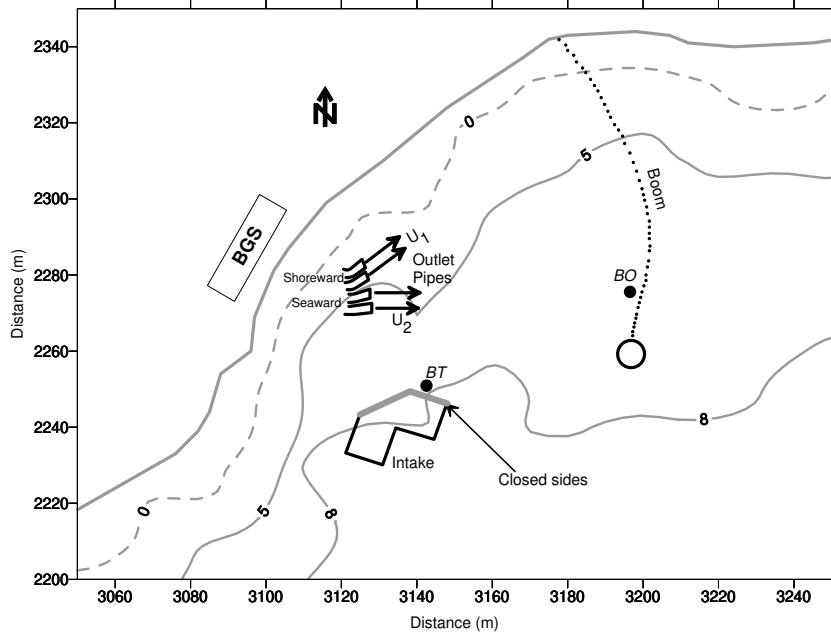


**Figure 2.** Enlarged map in the near-field of the outlet and intake. Symbols are the same as Figure 1. The boom is limited to the surface and has little or no effect on the flows below ~1 m depth.

**Methodology**

*Governing Equations*

The model solves the full three-dimensional, shallow water hydrodynamic and thermodynamic equations in a terrain following sigma-coordinate system (Blumberg and Mellor, 1987). The continuity, momentum, thermal energy and salinity equations, respectively are

Continuity equation:

$$\frac{\partial \zeta}{\partial t} + \int_{-1}^{0}\left(\frac{\partial Hu}{\partial x} + \frac{\partial Hv}{\partial y}\right)d\sigma = \int_{-1}^{0} qd\sigma \tag{1}$$

3

Reynolds momentum equation in the *x*-direction:

$$\frac{\partial u}{\partial t}+u\frac{\partial u}{\partial x}+v\frac{\partial u}{\partial y}+\omega\frac{\partial u}{\partial\sigma}-fv=-g\frac{\partial\zeta}{\partial x}-\frac{gH}{\rho}\int_{\sigma}^{0}\frac{\partial\rho}{\partial x}d\sigma$$
$$-\frac{g}{\rho}\frac{\partial H}{\partial x}\left(\sigma\rho+\int_{\sigma}^{0}\rho\,d\sigma\right)+\left[\frac{\partial}{\partial x}\left(A_x\frac{\partial u}{\partial x}\right)+\frac{\partial}{\partial y}\left(A_y\frac{\partial u}{\partial y}\right)\right]+\frac{1}{H}\frac{\partial}{\partial\sigma}\left(\frac{A_v}{H}\frac{\partial u}{\partial\sigma}\right)$$

(2)

Reynolds momentum equation in the *y*-direction:

$$\frac{\partial v}{\partial t}+u\frac{\partial v}{\partial x}+v\frac{\partial v}{\partial y}+\omega\frac{\partial v}{\partial\sigma}+fu=-g\frac{\partial\zeta}{\partial y}-\frac{gH}{\rho}\int_{\sigma}^{0}\frac{\partial\rho}{\partial y}d\sigma$$
$$-\frac{g}{\rho}\frac{\partial H}{\partial y}\left(\sigma\rho+\int_{\sigma}^{0}\rho\,d\sigma\right)+\left[\frac{\partial}{\partial x}\left(A_x\frac{\partial v}{\partial x}\right)+\frac{\partial}{\partial y}\left(A_y\frac{\partial v}{\partial y}\right)\right]+\frac{1}{H}\frac{\partial}{\partial\sigma}\left(\frac{A_v}{H}\frac{\partial v}{\partial\sigma}\right)$$

(3)

Conservation equation for temperature:

$$\frac{\partial T}{\partial t}+u\frac{\partial T}{\partial x}+v\frac{\partial T}{\partial y}+\omega\frac{\partial T}{\partial\sigma}=$$
$$\left[\frac{\partial}{\partial x}\left(D_x\frac{\partial T}{\partial x}\right)+\frac{\partial}{\partial y}\left(D_y\frac{\partial T}{\partial y}\right)\right]+\frac{1}{H}\frac{\partial}{\partial\sigma}\left(\frac{D_v}{H}\frac{\partial T}{\partial\sigma}\right)+\frac{Q_t}{\rho c_p H}$$

(4)

Conservation equation for salinity:

$$\frac{\partial s}{\partial t}+u\frac{\partial s}{\partial x}+v\frac{\partial s}{\partial y}+\omega\frac{\partial s}{\partial\sigma}=\frac{\partial}{\partial x}\left(D_x\frac{\partial s}{\partial x}\right)+\frac{\partial}{\partial y}\left(D_y\frac{\partial s}{\partial y}\right)+\frac{1}{H}\frac{\partial}{\partial\sigma}\left(\frac{D_v}{H}\frac{\partial s}{\partial\sigma}\right)$$

(5)

where $u$, $v$ and $\omega$ are the flow velocity components in the $x$, $y$ and $\sigma$ directions, respectively, $t$ is the time, $q$ is the source or sink of mass, g is the gravitational acceleration, $\zeta$ is the instantaneous water surface elevation, $H$ is the total water depth, $H=\zeta+h$, with $h$ denoting the undisturbed water depth, $f$ is the Coriolis parameter, $\rho$ is the fluid density, $A_x$ and $A_y$ are the horizontal turbulent momentum diffusion coefficients in the $x$ and $y$ directions, respectively, $A_v$ is the vertical turbulent momentum diffusion coefficient, $T$ is the temperature, $s$ is the salinity, $D_x$ and $D_y$ are the horizontal mass diffusion coefficients in the $x$ and $y$ directions, respectively, $D_v$ is the vertical mass diffusion coefficient, $Q_t$ is the thermal source or sink, and $c_p$ is the specific heat of sea water.

A second order turbulence closure model, as described in Mello and Yamada (1982), is applied to calculate the vertical momentum and mass diffusion coefficients, $A_v$ and $D_v$. The horizontal diffusion coefficients, $A_x$ and $A_y$, are evaluated using

Smagorinsky's formula (Smagorinsky, 1963). The vertical velocity in the σ-coordinate, ω, is determined according to

$$\omega = \frac{D\sigma}{Dt} = \frac{1}{H}\left[ -\int_{-1}^{\sigma}\left(\frac{\partial Hu}{\partial x} + \frac{\partial Hv}{\partial y}\right)d\sigma + \right.$$
$$\left. (1+\sigma)\int_{-1}^{0}\left(\frac{\partial Hu}{\partial x} + \frac{\partial Hv}{\partial y}\right)d\sigma + \int_{-1}^{\sigma}qd\sigma - (1+\sigma)\int_{-1}^{0}qd\sigma \right]$$

(6)

### Boundary Conditions

The boundary conditions of zero surface momentum flux (no wind stress) and bottom shear stress, as expressed in terms of a quadratic law, are employed. At the open boundaries, the water surface elevations are specified from measurements. Under inflows, open boundary conditions of temperature and salinity are specified using observed data, while for outflows, the conventional Sommerfeld radiation condition is applied (Sommerfeld, 1949).

### Solution techniques

The governing equations (1) − (5) are solved by a semi-implicit finite difference method in a staggered C-grid, which discretizes the convective and horizontal diffusive terms by an Eulerian-Lagrangian scheme (Casulli and Cattani, 1994), and the barotropic and vertical diffusive terms by an implicit method. Combining the differential continuity and momentum equations, a linear, five-diagonal system of equations for the water surface elevation, $\zeta$, is obtained as the following generalized form

$$a_{i,j}\,\zeta_{i,j}^{n+1} - a_{i+1/2,j}\,\zeta_{i+1,j}^{n+1} - a_{i-1/2,j}\,\zeta_{i-1,j}^{n+1} - a_{i,j+1/2}\,\zeta_{i,j+1}^{n+1} - a_{i,j-1/2}\,\zeta_{i,j-1}^{n+1} = b_{i,j} \qquad (7)$$

where $a$ and $b$ are the coefficients dependent on hydrodynamic properties at time step $n$, the subscripts $i$ and $j$ denote the horizontal location indices and the superscript $n$ represents the time step. This system is solved effectively by the pre-conditioned conjugate gradient method (Casulli and Cheng, 1992).

### Nested Grid Scheme

In the presence of a submerged buoyant jet, a much finer mesh in the near-field zone is required in order to resolve the sharp gradients in the hydrothermal field. Such mesh configuration can be accomplished using either unstructured grid or structured multi-grid methods. The unstructured-grid methods have shown impressive flexibility in grid refinement (Mavriplis, 1997), while existing structured multi-grid methods have limitations on high grid refinement as required by a buoyant jet. To obtain the necessary resolution for a buoyant jet using the latter method, one has to apply an adaptive multi-step grid scheme in that the hydrothermal field at each grid

has to be calculated in sequence (Berger and Colella, 1989), or an independent multi-block method in that the hydrothermal fields in the coarse and fine meshes are calculated separately and interpolated at the interfaces (Mavripli, 1992; Ramsey, *et al*., 1996). To overcome the above limitations, a new nested grid scheme is applied in ASL-COCIRM, where the near-field zone of the cooling water buoyant jet, as well as the intake, is embedded within the far-field zone using an extremely high resolution model grid, and these two zones are coupled together at their interfaces. The coupled system of hydrothermal equations is then solved at the same time in the complete field. The nested domain has the spatial grid sizes of $dx' = dx/L$ and $dy' = dy/L$, with $dx$ and $dy$ denoting the spatial grid sizes of the main-domain and $L$ representing the sub-divided step. This approach removes the constraint in a structured mesh on grid refinement and can apply extremely high refinement at a single step. It therefore reduces the coupled interfaces, and at the same time, allows realistic computation of the large gradients in the hydrothermal properties.

Inside the nested-domain, the differential continuity, momentum and thermal conservation equations are the same as in the main-domain. At the interfaces, a coupling scheme is applied in terms of mass, momentum and thermal conservation. To ensure momentum, heat and salinity conservation, the flux forms of the momentum and thermal conservation equations are applied at the interface. By considering mass conservation at the interfaces, the resulting continuity equations are related to both the nested-domain and the main-domain grid points. The generalized continuity equations at nested-domain interior grid points and interface grid points, as shown in Figure 3, are given in Eqs. (8) − (10), respectively. The differential continuity equations at other interfaces will have similar forms.
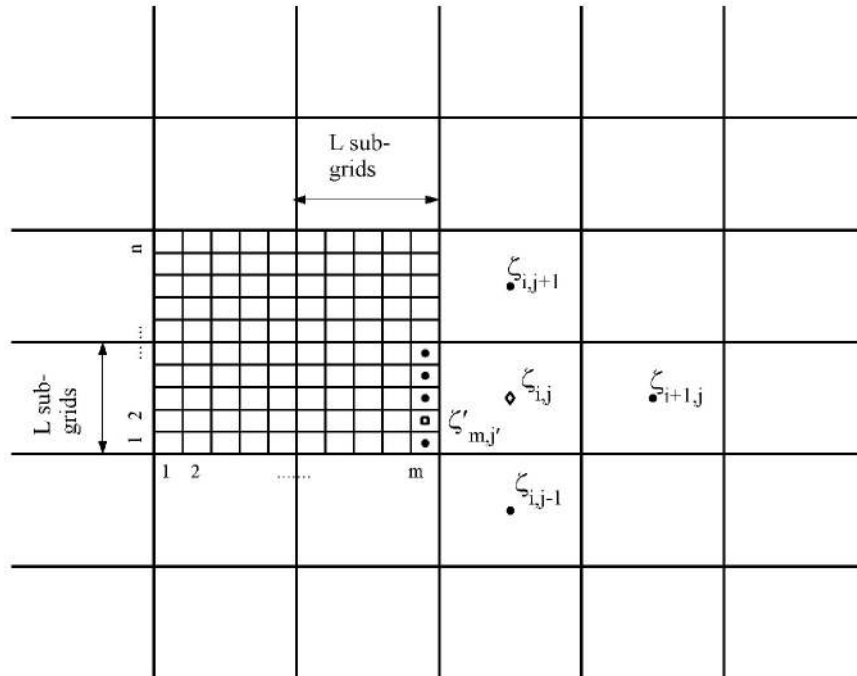


**Figure 3.** Schematic diagram showing nested-grid.

The interior grid point in the nested-domain:

$$a'_{i',j'}\,\zeta'^{n+1}_{i',j'} - a'_{i'+1/2,j'}\,\zeta'^{n+1}_{i'+1,j'} - a'_{i'-1/2,j'}\,\zeta'^{n+1}_{i'-1,j'} - a'_{i',j'+1/2}\,\zeta'^{n+1}_{i',j'+1} - a'_{i',j'-1/2}\,\zeta'^{n+1}_{i',j'-1} = b'_{i',j'} \quad (8)$$

The interface grid point at the nested-domain side (square point in Figure 3):

$$
\begin{aligned}
&\left( a'^{it}_{m,2} + \frac{2a'_{m+1/2,2}}{L+1} \right)\zeta'^{n+1}_{m,2} - a'_{m-1/2,2}\,\zeta'^{n+1}_{m-1,2} - a'_{m,2+1/2}\,\zeta'^{n+1}_{m,3} - a'_{m,2-1/2}\,\zeta'^{n+1}_{m,1} - \\
&\left( \frac{2a'_{m+1/2,2}}{L+1} \right)\left( \beta'_{m+1/2,2}\zeta^{n+1}_{i,j-1} + \beta''_{m+1/2,2}\zeta^{n+1}_{i,j} + \beta'''_{m+1/2,2}\zeta^{n+1}_{i,j+1} \right) = b''_{m,2}
\end{aligned}
\quad (9)
$$

The interface grid point at the main-domain side (diamond point in Figure 3):

$$
\begin{aligned}
&\left[ a^{it}_{i,j} + \sum_{j'=1}^{L}\left( \beta''_{m+1/2,j'}\frac{2a'_{m+1/2,j'}}{L+1} \right) \right]\zeta^{n+1}_{i,j} - a_{i+1/2,j}\,\zeta^{n+1}_{i+1,j} - \\
&\sum_{j'=1}^{L}\left( \frac{2a'_{m+1/2,j'}}{L+1}\zeta'^{n+1}_{m,j'} \right) - \left[ a_{i,j+1/2} - \sum_{j'=1}^{L}\left( \beta'''_{m+1/2,j'}\frac{2a'_{m+1/2,j'}}{L+1} \right) \right]\zeta^{n+1}_{i,j+1} - \\
&\left[ a_{i,j-1/2} - \sum_{j'=1}^{L}\left( \beta'_{m+1/2,j'}\frac{2a'_{m+1/2,j'}}{L+1} \right) \right]\zeta^{n+1}_{i,j-1} = b''_{i,j}
\end{aligned}
\quad (10)
$$

where $a'$ and $b'$ are the coefficients derived from embedded grid, $\zeta'$ is the water surface elevation at the cell centers of the nested-domain, $b''$ is the combined coefficient of both the main and embedded grids at the interface, $\beta$ is the weighting coefficient, with $\beta' + \beta'' + \beta''' = 1$, and $a^{it}$ is a coefficient excluding the interface side, e.g., $a'^{it}_{m,2} = 1 + a'_{m-1/2,2} + a'_{m,2+1/2} + a'_{m,2-1/2}$ in Eq. (9) and $a^{it}_{i,j} = 1 + a_{i+1/2,j} + a_{i,j+1/2} + a_{i,j-1/2}$ in Eq. (10). Although the resulting differential continuity equations at the interface involve more than 5 grid points, with 7 points at the nested-domain interface grid [Eq. (9)] and $(4+L)$ points at the main-domain interface grid [Eq. (10)], the differential Equations (7) – (10) are combined into a positive-definite linear system, and therefore, have an unique solution. Thus, the combined linear system is solved by the pre-conditioned conjugate gradient method in all grid cells and every time step with a single modeling procedure.

The buoyant jet entrainment and diffusion are represented in the model by Smagorinsky's formulation and the second order turbulence closure model. The Smagorinsky formula represents the horizontal diffusion as a function of velocity shear (Smagorinsky, 1963). To ensure that the buoyant jet entrainment will be represented appropriately in the 3D model, the Smagorinsky coefficient was adjusted in order that the jet entrainment agreed with the empirical formulation of Bemporad (1994). Further details on this optimization can be found in Jiang, et al. (2003). In the

turbulence closure model, all empirical constants were assigned the values reported in Mellor and Yamada (1982).

In the present application, the main far-field domain included the whole area of Port Moody Arm from the mouth at Burrard Inlet (Figure 1), and was resolved using a grid-size measuring 50 m × 50 m with 10 equally spaced vertical sigma-layers. The nested near-field domain covers an area of 300×200 m$^2$ (Figure 1) with $L$=20, which results in a horizontal resolution of 2.5 m × 2.5 m and represents the cooling water outlet and intake in a realistic manner (Figures 4 and 5). It has the same vertical layers as the main-domain. Within the nested domain, selected cells of the equivalent area are used to represent the outlet pipes, i.e., 4.67 m$^2$ for each individual pipe (Jiang, *et al*., 2002). By specifying the jet discharge, exit temperature and salinity in these cells, the tidal mean thermal flux and momentum are approximately equal to the actual thermal flux and momentum in the outlet pipes.
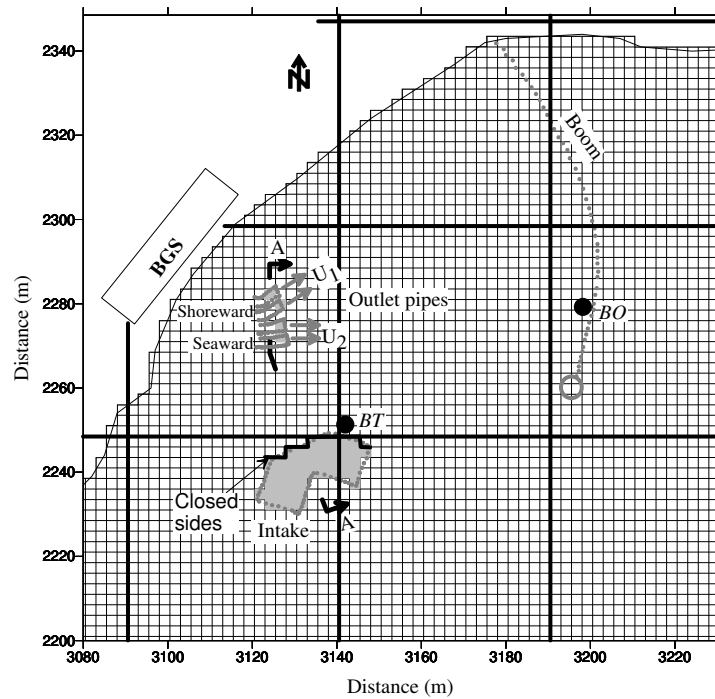


**Figure 4.** Numerical plane mesh (thin lines for nested-grid and thick lines for main-grid) at the near-field.
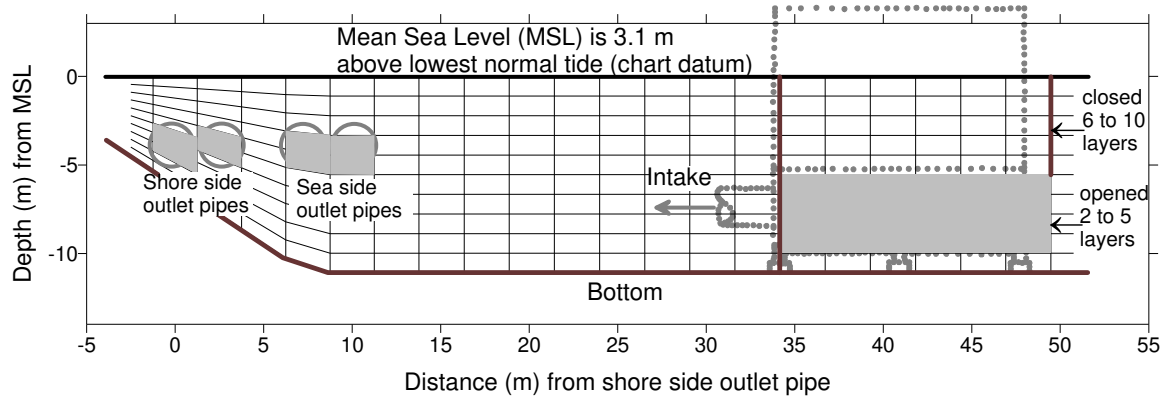
8

**Figure 5.** Vertical location of outlet and intake in numerical mesh grid along A–A cross-section (Figure 4).

## Model Results

### *Model Calibration and Verification*

Extensive model calibrations and verifications were carried out before examining the potential recirculation of the waste heat into the intake. At first, the simulated buoyant jet was calibrated and verified with an empirical relationship of jet entrainment (Bemporda, 1994) and an integral 1D model (Johnston, et al., 1994) to compute buoyant jet trajectory, dilution and impinging location at the surface. The integral model solves the radially integrated conservation equations following the jet axis. The jet entrainment was calibrated for the simple case of a neutrally buoyant jet discharging into a stagnant homogenous environment. The neutral jet was set at 4 m above bottom with an outlet velocity of 2 m/s. The empirical Smagorinsky coefficient was adjusted until the simulated entrainment rate realized a best fit with the empirical relationship. The correlation coefficient between modeled and empirical entrainment rates is found to be 0.89 (Jiang, et al., 2003). The model was then run with the optimized Smagorinsky coefficient for a buoyant jet discharging into a stagnant environment of typical summer stratification, with a cooling water discharge of 19.6 m$^3$/s, outlet velocity of $U_2$ = 2.0 m/s and outlet temperature of 26 °C. Figure 6 compares the numerical model outputs in the nested grid area with the corresponding integral model results and field measurement. It is seen that the model reproduces the buoyant jet trajectory, dilution and impinging location in a realistic fashion.
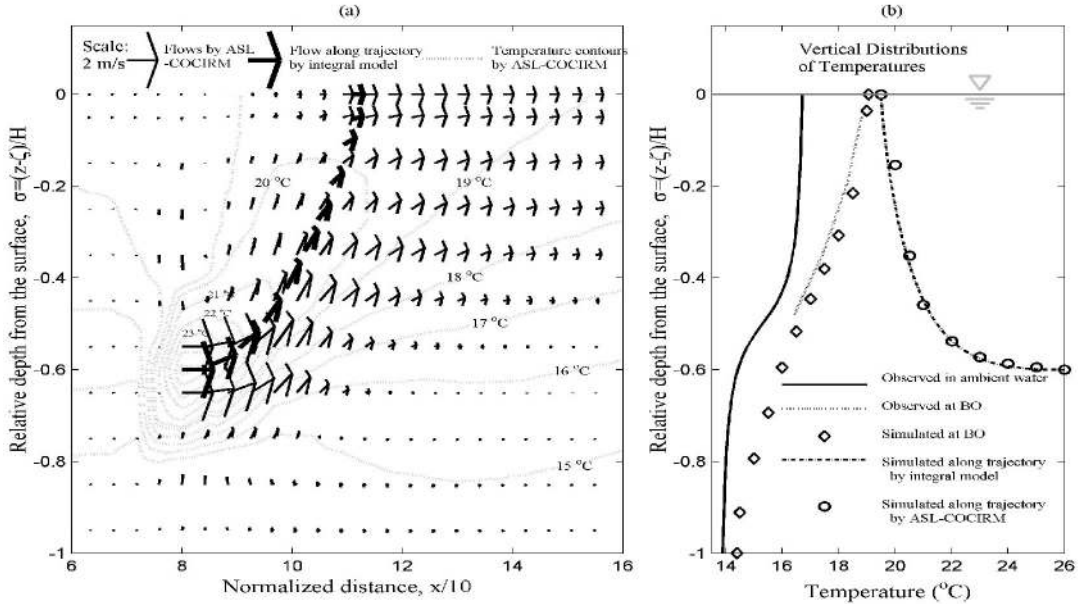
**FIGURE 6.** Buoyant jet (a) and vertical structures of temperatures (b).

The flow pattern around the buoyant jet was verified using historical dye tracing data (Hodgins and Webb, 1991; Jiang, et al., 2003). Modeled temperature profiles in the near-field, at the sites BT and BO as shown in Figure 2, were then compared with *in situ* observations to demonstrate the model's ability to reproduce the thermal field (Figures 7 and 8). The overall agreement between simulations and observations is very good (Figure 8), with the correlation coefficient of modeled versus observed results up to 0.95 or better (Jiang, et al., 2003), except at surface levels where the effect of wind mixing as a shallow surface layer of 2 – 4 m is not reflected in the model (which did not include wind inputs).
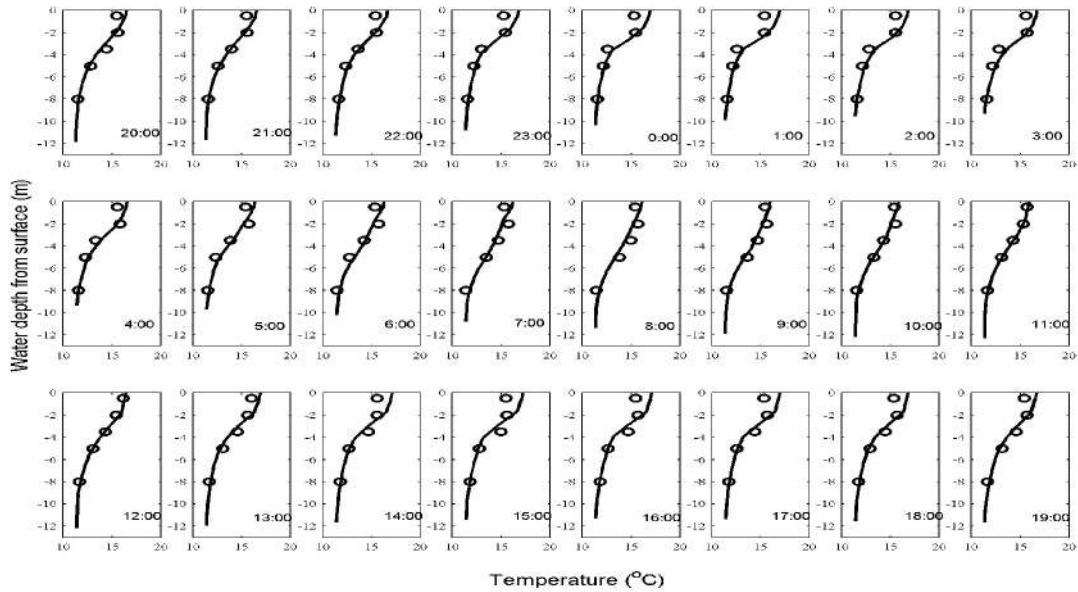


**Figure 7.** Comparison between simulated (solid lines) and observed (open circles) temperature profiles at BT (see Figure 2 for location) for October 24 – 25, 1998.
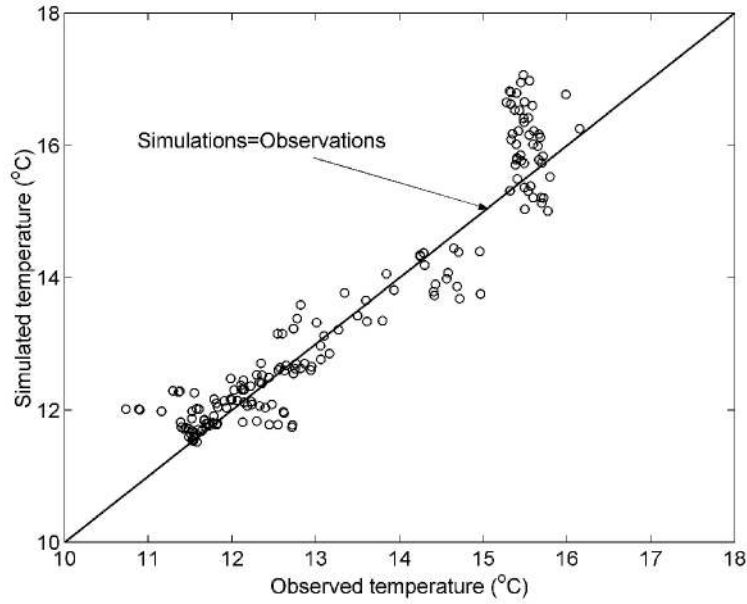
10

**Figure 8.** Simulated temperatures as a function of observations at survey elevations for the same site and period in Figure 7.

### Cooling Water Recirculation

The simulated flows in the near field show no evident direct recirculation of the cooling water (Jiang, et al., 2001). Water flows at the intake structure are from the SW during flood tide, and originate from the east during ebb tide. Because of the higher water temperatures at the eastern side (Figure 9), which faces the buoyant jet, it is expected that cooling water intake temperature increases during ebb tide. However, the horizontal gradient of water temperature decreases with increasing water depth and is almost reduced to zero at depths below the stratification layer (Figure 7). Therefore, the effect of intake flow direction on cooling water intake temperature could be significant only as the water depth at the intake is reduced (i.e. at low tide) or the deeper part of the thermocline layer extends downward to the levels of the plant input flows. This condition could happen during the ebb of large tide when the intake takes warmer water not only from the eastern side but also from the deeper part of the thermocline layer. Such possible indirect recirculation is examined using the averaged cooling water intake temperature ($T_{in}$), a key plant operational parameter, which is defined as

$$
T_{in} = \frac{\sum\limits_{k=1}^{K}\left[\int\limits_{1.54}^{5.88} T_k(z)q_k(z)dz\right]}{\sum\limits_{k=1}^{K}\left[\int\limits_{1.54}^{5.88} q_k(z)dz\right]}
\tag{11}
$$

11

where *K* is all the grid sides surrounding around the intake structure, the limits of integration mean the intake opening heights (m) above the bottom. $T_k(z)$ and $q_k(z)$ are respectively the simulated temperature and discharge profiles at each side, which are obtained through transformation of simulated temperature and discharge in σ-coordinate into *z*-coordinate.

The modeled results reveal considerable variations of cooling water intake temperature during large tides (Jiang, et al., 2001), and are in reasonable agreement with the data measured in the intake water mixing box (not shown). Typically, the cooling water intake temperature increases during ebb tide and reaches peak values at around low water (Figure 9). As the water level rises, temperatures decrease again. The variations of 0.3 – 1.0 ℃ are found in fall and winter seasons, and 1.0 – 1.5 ℃ variation for summer season (Jiang, et al., 2001). It is also observed that the variation of cooling water intake temperature appears to be very minor during low tide (Figure 9).
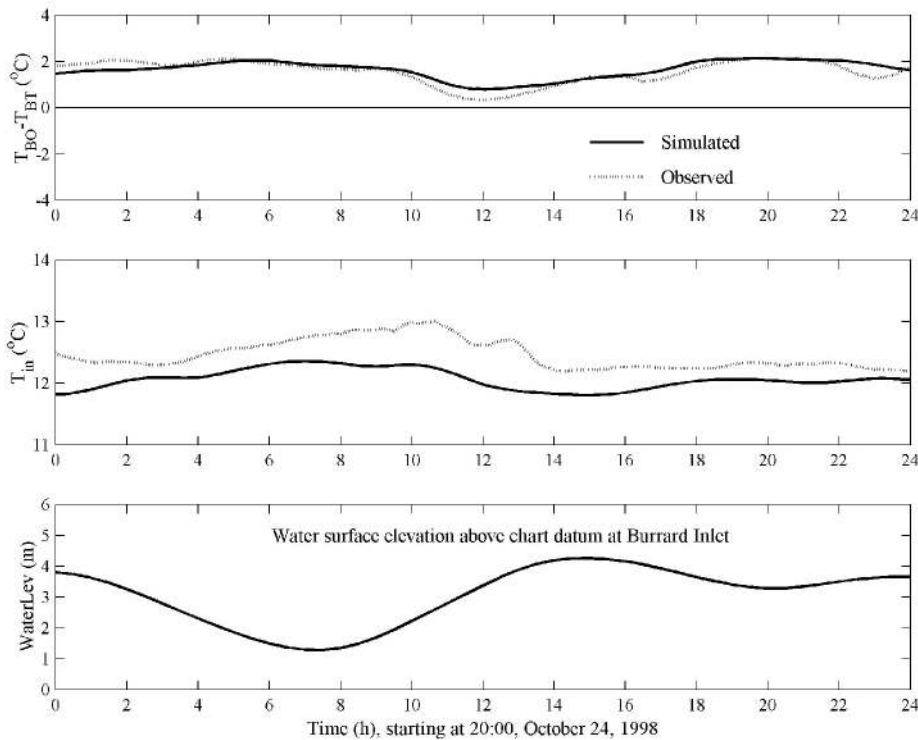


**Figure 9.** Comparisons between simulated and observed temperature gradients at 5 m depth and the cooling water intake temperature.

As stated above, this feature is mainly caused by stratification (or thermocline) of the vertical profile in water temperature, as shown in Figure 7. During summer (May – September), the thermocline penetrates to greater water depths (to 5 m but less than 8 m depth) and warmer water is found at the top layers and in the eastern side of the intake as well. As water depth decreases dramatically during the ebb from high tide, the thermocline is drawn down to the intake openings with the result that warmer water is taken into the cooling water system. As a result, the cooling water intake temperature gradually increases and reaches peak values

around the time of low water, while it decreases over the flood tide. After summer, this effect becomes weaker because the thermocline is closer to the sea surface and further from the intake depths. Thus, there is less variability in cooling water intake temperature with tidal periods, as seen in the October simulation (Figure 9). During winter, this feature could be reversed, dependent on plant output and atmospheric conditions. For extreme weather conditions with air temperature well below zero °C, colder water occurs in the top layers most of the time, which is associated with salinity stratification at the top layers. As a consequence, the intake will take some colder water from the upper layers into the cooling water system when water depth decreases during ebb tide and has lower temperature. As the water depth increases during flood tide, it mainly takes warmer water from the near-bottom layers and has slightly higher temperature.

To better understand the simulated results, the relationship between the measured cooling water intake temperature, $T_{in}$, and water surface elevation were examined (Figure 10). It is observed that "low" $T_{in}$, which is defined here as the value at the "trough" of $T_{in}$ tidal variation, occurs during high water, and lower values are usually found during higher high water (HHW) than during lower high water (LHW). While, the majority of peak values of $T_{in}$, defined in an analogous way as the value at the crest of $T_{in}$ tidal variation, occurs during low water, usually with a higher value during lower low water (LLW) than during higher low water (HLW). Some maximum $T_{in}$ occurs during low water with a lag of $0.5 - 1.5$ hour (Figure 10). Therefore, the observations of cooling water intake temperature replicate the simulated results as stated above.
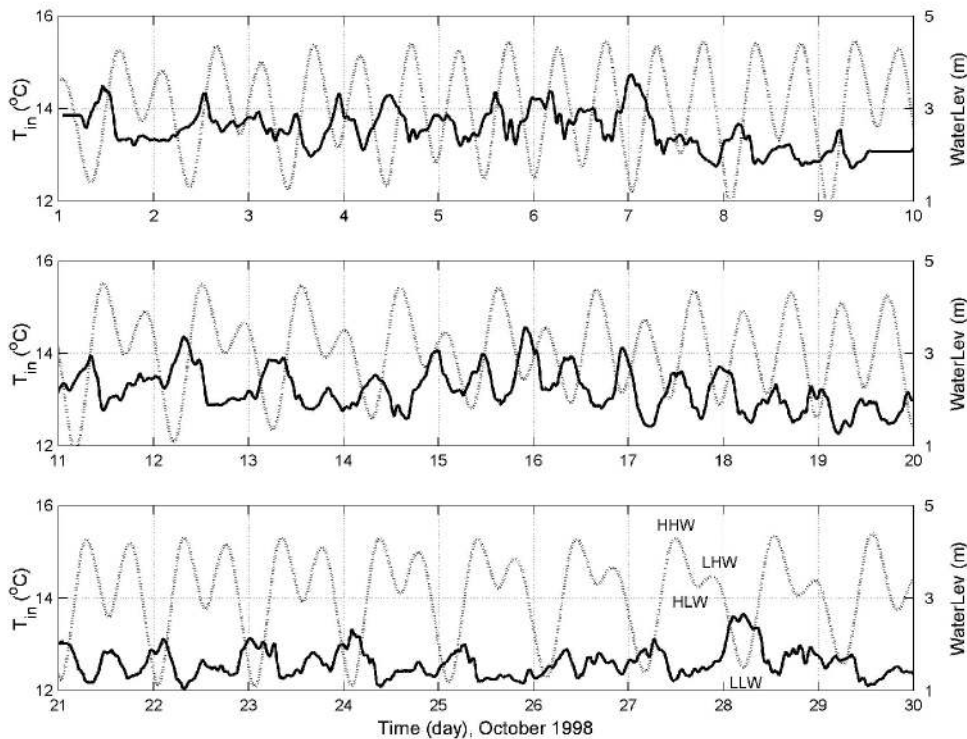


**Figure 10.** Measured cooling water intake temperature (solid line) and water elevation (dotted line) in October 1998.

**Conclusion**

The newly-developed nested grid scheme in ASL-COCIRM allows extremely high grid refinement at a single step. Such an approach is useful in representing the hydrothermal properties for a cooling water structure in a realistic manner and resolving the large gradients in the hydrothermal field in the presence of a submerged buoyant jet. By coupling the far-field and near-field and solving the complete zone in a single modeling procedure, the model is capable of adequately capturing the overall behavior of the buoyant jet at every time step and quantitatively examining the possible cooling water recirculation into the intake.

In the current application to model Burrard Generating Station cooling water recirculation, there was no direct evidence of any recirculation occurring. However, depending on the vertical structure of temperature, upper warmer stratified layers could be mixed down to the intake opening and be taken in as cooling water during low water. It is shown that cooling water intake temperatures increase during ebb tide and reach peak values around low tide, and decrease during flood tide. The lowest values of cooling water intake temperatures occur at high water. This effect is most significant during summer and becomes weaker in the fall and winter seasons. Generally, cooling water intake temperatures in summer are about $1.0 - 1.5$ °C colder at higher high water than that at lower low water and about $0.3 - 1.0$ °C colder in fall and winter seasons, for similar tidal conditions.

**Acknowledgements**

**References**

Bemporad, G. A. (1994). "Simulation of round buoyant jet in stratified flowing environment." *Journal of Hydraulic Engineering*, ASCE, 120, 529-543.

Berger, M. J., and Colella, P. (1989). "Local adaptive mesh refinement for shock hydrodynamics." *Journal of Computational Physics*, 82, 64-84.

Birtwell, K. L., Brotherston, A. E., Fink, R. P., Fissel, D. B., Greenbank, J. D., Heithaus, L. I., Korstrom, J. S. and Taylor, A. E. (2001). *Thermal Inputs into Port Moody Arm*, *Burrard Inlet*, *BC*, *and Effects on Salmon*: *a Summary Report*. Canadian Technical Report of Fisheries and Aquatic Sciences 2340, p35.

Blumberg, A. F., and Mellor, G. L. (1987). "A description of a three-dimensional coastal ocean circulation model." In: *Three-Dimensional Coastal Ocean Models*, N. S. Heaps ed., American Geophysical Union, Washington, DC, 1-16.

Casulli, V., and Cattani, E. (1994). "Stability, accuracy and efficiency of a semi-implicit method for three-dimensional shallow water flow." *Computers & Mathematics with Applications*, 27, 99-112.

Casulli, V., and Cheng, R. T. (1992). "Semi-implicit finite-difference method for three-dimensional shallow water flow." *International Journal for Numerical Methods in Fluids*, 15, 629-648.

Fissel, D. B., MacNeil, M., and Taylor, A. E. (1998). *A Study of the Thermal Regime of Port Moody Arm in Relation to the Burrard Thermal Generating Station*. ASL Technical Report, ASL Environmental Sciences Inc., Sidney, BC, Canada, 64p.

Hodgins, D. O., and Webb, A. J. (1991). *Determination of Residual Chlorine in Burrard Inlet Originating from the Burrard Thermal Generating Plant*. Technical Report, Seaconsult Marine Research Ltd., Vancouver, BC, Canada, 55p

Jiang, J., Fissel, D. B., Lemon, D. D., and Topham, D. (2002). "Modeling cooling water discharges from the Burrard Generating Station, BC Canada." *Proceedings of Oceans 2002 MTS/IEEE*, Biloxi, Mississippi, USA, 1515-1521.

Jiang, J., Fissel, D. B., and Taylor, A. E. (2001). *Burrard Generating Station Cooling Water Recirculation Study*. ASL Technical Report, ASL Environmental Sciences Inc., Sidney, BC, Canada, 45p.

Jiang, J., Fissel, D. B., and Topham, D. (2003). "3D numerical modeling of circulations associated with a submerged buoyant jet in a shallow coastal environment." *Estuarine, Coastal and Shelf Science*, 58, 475-486.

Johnston, A. J., Phillips, C. R., and Volker, R. E. (1994). "Modeling horizontal round buoyant jet in a shallow water." *Journal of Hydraulic Engineering*, ASCE, 120, 41-59.

Mavriplis, D. J. (1992). "Three-dimensional multi-grid for the Euler equations." *AIAA Journal*, 30, 1753-1761.

Mavriplis, D. J. (1997). "Unstructured grid techniques." *Annual Review of Fluid Mechanics*, 29, 473-514.

Mellor, G. L., and Yamada, T. (1982). "Development of a turbulence closure model for geographical fluid problems." *Review of Geophysics*, 20, 851-875.

Ramsey, J. S., Hamilton, R. P., and Aubrey, D. G. (1996). "Nested three-dimensional hydrodynamic modeling of the Delaware Estuary." In: *Proceeding of the 4th International Conference on the Estuarine and Coastal Modeling*, ASCE Waterway, Port Coastal and Ocean Division, 53-65.

Smagorinsky, J. (1963). "General circulation experiments with the primitive equations: I. The basic experiment." *Monthly Weather Review*, 91, 99-164.

Sommerfeld, A. (1949). "Partial differential Equations." *Lectures in Theoretical Physics*, Vol. 6, Academic Press.

Taylor, A. E. and Fissel, D. B. (1999). *A study of the thermal regime of Port Moody Arm*, *Volume I*. ASL Technical Report, ASL Environmental Sciences, Sidney, BC, Canada, 50p + figures and appendices.